

In-Situ Qualification and Physics-Based Process Design for Aerosol Jet Printing via Spatially Correlated Light Scattering Measurements

Jeremy D. Rurup^a, Ethan B. Secor^{a,}*

^a Department of Mechanical Engineering, Iowa State University, Ames, IA 50011, USA

* Correspondence to: Iowa State University, Ames, IA 50011, USA. E-mail address: esecor@iastate.edu.

HIGHLIGHTS

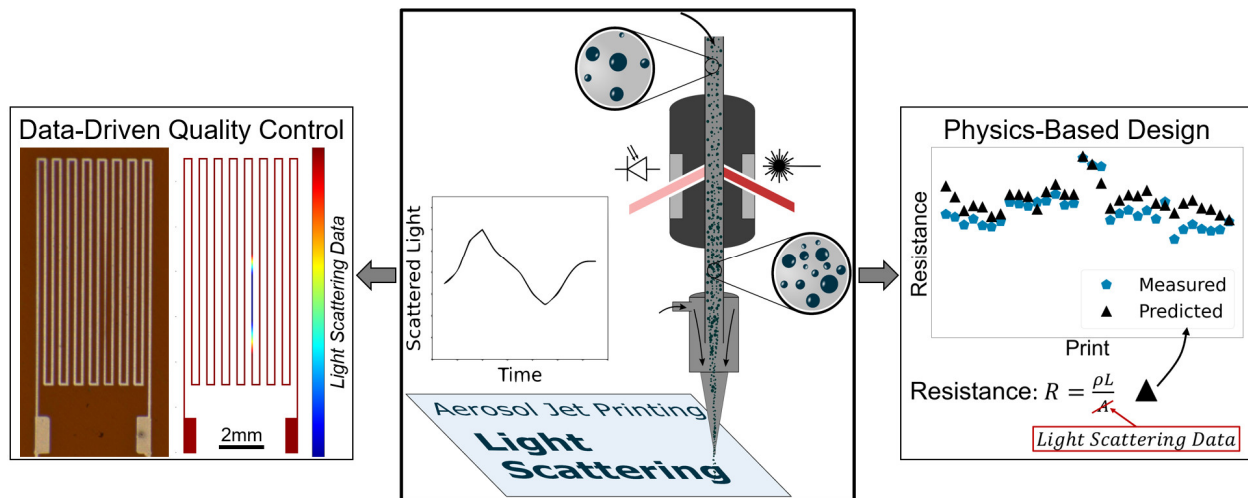
- Employed optical measurements for in-situ qualification of aerosol jet printing
- Mapped deposition rate to positional coordinates with sub-second precision
- Predicted bulk electrical properties using real-time light scattering data
- Demonstrated automatic repair of defects in printed features

ABSTRACT

Aerosol jet printing is a contactless, digital, and additive technique broadly used for manufacturing flexible, hybrid, and conformal electronics. However, both intra-batch and batch-to-batch variability have hindered widespread industry adoption and scaling to production volumes. Recently, light scattering measurements have emerged as a tool to measure aerosol volume fraction – a key parameter determining deposition rate – and have proven an effective feedback source for closed-loop control on timescales ranging from tens of minutes to hours. While this is a promising capability to mitigate long-term process drift, it lacks the temporal

resolution to validate print quality for complex and precise electronic circuits. Here, real-time process monitoring with <1 s resolution is demonstrated for in-situ qualification of aerosol jet printing. To begin, the correlation between light scattering and aerosol deposition is validated at 500 ms time intervals, allowing deposition rate to be mapped to positional coordinates and providing a new data stream to drive quality control assessments. This allows optical scattering to be connected to electrical properties including line and sheet resistance, resulting in predictions nominally within 10% of measured values for sets of printed devices. Finally, the ability to spatially correlate print defects during fabrication is demonstrated as a foundation for a print repair framework, successfully repairing prints with randomly induced defects to achieve resistance within 5% of a control set.

GRAPHICAL ABSTRACT



KEYWORDS: additive manufacturing, printed electronics, process monitoring, hybrid electronics, digital manufacturing

ACKNOWLEDGEMENTS

The authors acknowledge Honeywell FM&T for funding support under PO N000478736, along with Northrop Grumman NG Next Research Laboratories. Honeywell FM&T is supported by the U.S. Department of Energy National Nuclear Security Administration under contract DE-NA0002839.

FUNDING

Funding to support this work was provided by Honeywell FM&T under PO N000478736. Honeywell FM&T is supported by the U.S. Department of Energy National Nuclear Security Administration under contract DE-NA0002839. Additional funding support for this work was provided by Northrop Grumman.

1. Introduction

Additive manufacturing (AM) techniques have become widely accepted across multiple manufacturing sectors, including aerospace, medical, energy, and automotive [1,2]. AM currently fills several important niches, allowing for on-demand production of intricate parts otherwise impossible or too costly with conventional methods, as well as rapid prototyping and low-volume production runs. However, the serial nature of AM production, combined with the complex interplay of machine parameters and resulting material properties and functional tolerances, makes component design and qualification a notable challenge [3]. In this regard, the inherently digital nature of AM offers a compelling route to establish a data-rich, intelligent manufacturing system to combat such difficulties. Within the field of printed electronics, aerosol jet printing (AJP) offers a promising technology for flexible and hybrid electronics manufacturing, with demonstrated devices spanning wireless communication [4–6], physical and chemical sensing [7–13], energy storage [14–16], and transistors [17,18], among others. AJP is a

non-contact, digital technique in which an aerosolized, liquid ink containing functional materials is transported to a printhead by a carrier gas stream. There, the aerosol stream is collimated by an annular sheath gas and directed through a nozzle onto the target substrate. Typical feature sizes range from 10-100 μm depending on the ink, hardware, and process setup. Printable materials typically span metallic nanoparticles [19] and polymers, but can also include semiconductors [20] and carbon-based inks [21,22]. The high nozzle-to-surface offset, resolution, and materials compatibility has made AJP popular in electronics packaging applications [23–25], as well as conformal printing on components with 3D surface topography [26–29], including additively manufactured polymeric substrates [30,31].

Despite its promise, AJP currently lacks adequate tools to design and qualify prints commensurate with the requirements and expectations of the electronics fabrication industry. Setting up an aerosol jet print to achieve a target geometry or bulk property, such as thickness or sheet resistance, is an empirical, largely manual, and iterative process. Even with an experienced operator familiar with both the printer and the particular ink, the amount of material deposited remains unknown until after print completion, post-processing, and off-line measurement, and can moreover exhibit significant variation within the time scale of typical production runs [32]. In recent years, several techniques have been proposed to address these shortcomings, especially with regard to reducing process drift. Automated imaging techniques have been applied to detect variations in printed line width [33,34]. While this can be a sufficient quality control measure in some applications, printed line width and the true deposition rate are not in general directly correlated, and multi-layer printing on disparate materials can confound imaging-based inspection [35]. Gu et al. deposited aerosol droplets into inkwells etched into a silicon wafer to quantify a wet deposition rate [36]. The deposition rate was estimated by the inkwell volume and

fill time, based on a user observation, providing feedback for the operator to tune printing parameters. Using a different approach, Salary et al. investigated an in-situ, post-deposition imaging method, estimating feature heights with a shape-from-shading algorithm [37,38]. This data stream was later combined with a closed-loop control algorithm to maintain constant deposition rate [39].

All of these methods are key advancements offering a new source of data on deposition rate, but they remain unable to provide data in real time. While drift occurs over extended time scales (minutes to hours), AJP is also susceptible to variations in deposition rate over shorter timescales. Applications with strict requirements for electrical resistance or thickness require a rigorous and robust quality control technique focused on the deposition rate. In pursuit of this goal, optical extinction and scattering methods have been developed for real-time monitoring, with deposition rate showing a strong linear relationship with optical power measurements [40,41]. Most recently, Rurup et al. demonstrated a closed-loop control architecture employing light scattering measurements as a feedback source [42]. While this work effectively mitigated long-term drift during deposition, allowing for reliable average output on time scales of tens of minutes to hours, it neglects short-term variability. Addressing this blind spot is crucial for electronics production, for which a rapid but severe printing defect can result in an open or shorted electrical connection. Machine operators require information on the position, magnitude, and duration of defects to assess their impact on electrical functionality. With this refined data, operators can make an informed decision to scrap a part with a critical defect, attempt repair, or continue to the next production step if the defect occurs in a non-critical region. This unmet need for AJP is the focus of the present work – with the same hardware concept as previous work, but

using the data within a more sophisticated platform to enable a qualitative advance in the confidence and precision of quality control.

Here, light scattering measurements are shown to provide physically meaningful data regarding the deposition rate over short time scales, enabling tools for enhanced qualification, physics-based process design, and even defect repair for AJP parts. To lay the foundation for this work, a strong linear correlation between optical scattering and physical properties – cross-sectional area and electrical conductance – is validated within a print lasting only 10 s, with scattering data recorded at <1 s intervals. Precision at this measurement frequency enables high-fidelity prediction of deposition rate within prints, rather than averaging over printed samples, including correlating the measurements spatially within the printed part. Because light scattering is a proxy for the aerosol volume fraction, a fundamental contributor to the deposition rate or mass flux, scattering measurements can be substituted into equations for electrical resistance and sheet resistance. This methodology is experimentally validated, and enables a mutable, physics-driven approach to predicting electrical properties of printed devices, thus allowing a new method of in-situ qualification for AJP. Additionally, the sub-second precision of scattering measurements is harnessed to demonstrate, for the first time, an automated repair technique, selectively adding material to under-filled regions of a printed sample. Altogether, this work demonstrates a fundamental methodology to enable more rigorous and efficient procedures for design and qualification of aerosol jet printed parts in production and research environments.

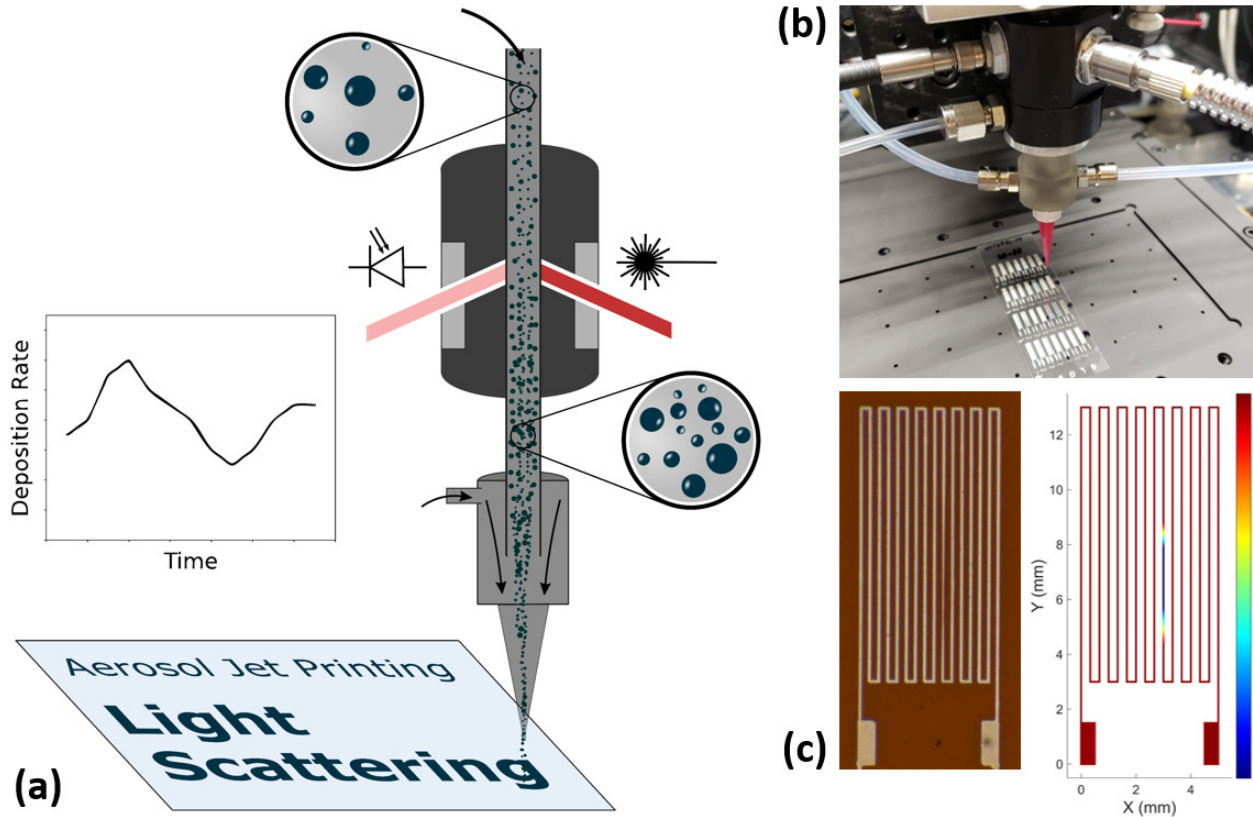


Fig. 1. (a) Diagram of an aerosol jet printer equipped with an optics cell to measure light scattered by aerosol droplets, enabling real-time detection of deposition rate. (b) Image of the optics cell hardware and fiber optic cables installed on the printer, immediately upstream of the flow cell and nozzle. (c) An image of a serpentine pattern printed via AJP (right), with its corresponding colormap depicting the light scattering measurements plotted at XY coordinates (left) indicating a region with inadequate material deposition.

2. Theoretical Foundations

2.1. Deposition Rate

Aerosol jet printing is an additive technique, and thus the amount of material deposited will impact the geometrical and functional characteristics of the final printed device. Here, the deposition rate of solid material for AJP is defined as

$$r_{dep} = v_a f_a \chi_s \eta_{imp} \quad (1)$$

in which the deposition rate (r_{dep} , $\text{m}^3 \text{s}^{-1}$) is a product of the volume fraction of aerosol in the carrier stream (v_a), the carrier gas flow rate (f_a , $\text{m}^3 \text{s}^{-1}$), the ink solids volume fraction (χ_s), and the impaction efficiency of droplets exiting the nozzle (η_{imp}) [40]. As Tafoya et al. note, porosity in the printed sample can certainly affect cross-sectional area or volume measurements, but this effect is independent of the true deposition rate.

Variability in deposition rate poses a significant challenge for print validation and quality control, particularly when attempting to maintain strict manufacturing tolerances on thickness or resistance [43]. Some parameters of (1) are relatively straightforward to control, such as the carrier gas flow rate, which is set via precise mass flow controllers (within $\pm 1\%$ accuracy). The solids volume fraction of the ink can in principle vary slowly, but this can be mitigated with selection of low vapor pressure solvents or use of solvent add-back or bubbler systems [44]. Thus, the largest uncontrolled source of variability is the aerosol volume fraction. Aerosol droplets are generated via one of two atomization systems – ultrasonic or pneumatic. With ultrasonic atomizers, a piezoelectric transducer oscillating at high (MHz) frequency induces a capillary wave on the ink surface, resulting in droplet formation. With pneumatic atomizers, aerosol is generated by a high velocity gas flow directed over the liquid ink, as shear forces and fluid instabilities interact to produce droplets. Both methods result in a polydisperse aerosol, and the number and size of droplets generated is a complex and poorly understood outcome of many variables, with insufficient direct control. For AJP, ink composition, temperature, cartridge fill level, pressure, and many other parameters can influence atomization, posing a challenge for highly controlled production as well as systematic material development [32]. For the purposes of this study, the fact that neither technique allows for precise, in-situ control of the aerosol

volume fraction is a key motivator to monitor and, where possible, correct for variation in this important parameter.

2.2. Volume Fraction and Optical Scattering

In previous work, a linear relationship has been shown between the aerosol volume fraction (v_a) and the intensity of scattered light (P_{sc}), as described by (2) [41]. For aerosol jet printers equipped with ultrasonic atomizers, the droplet size distribution is expected to span approximately 1-5 μm [45]. Mie scattering dominates the interaction with visible and near infrared light for droplets in this range, and other scattering mechanisms applicable to a wider range of droplet size maintain proportionality of scattering with the number density of scatterers under dilute conditions. Precisely relating aerosol volume fraction and scattering power requires accurate information on the droplet size distribution at the instant of measurement, refractive index of the ink, and details of the measurement configuration [46], but the proportionality of aerosol volume fraction and scattering power is valuable in itself, as these ink- and process-specific parameters can be accounted for with appropriate calibration. Previous work has validated this for inks with distinct optical properties, spanning transparent solutions and optically dense colloidal dispersions, to confirm the proportionality of volume fraction with scattering power for the scope of materials relevant to AJP.

$$v_a \propto P_{sc} \quad (2)$$

To more practically align (2) with AJP, scattering power is substituted into (1), additionally normalizing to the feed rate, or print speed. This creates a generalizable process metric for inferring the deposition rate. This term is referred to as the linear deposition metric (LDM), and is defined as

$$LDM = \frac{P_{sc} f_a}{v_f} \quad (3)$$

where LDM is the linear deposition metric ($W\ m^2$), P_{sc} the scattering power (W), f_a the carrier gas flow rate ($m^3\ s^{-1}$), and v_f the feed rate ($m\ s^{-1}$). The LDM may be thought of as a proxy for the cross-sectional area, or more precisely as a representation of the volume of material deposited per unit length, with $\mu m^3/mm$ being an appropriate unit. Rurup et al. demonstrated a strong linear correlation between the LDM and the actual linear deposition rate, as expressed in (4) [42].

$$A = LDM * m_a + b_a \quad (4)$$

Here, A is the cross-sectional area (m^2), while m_a (W^{-1}) and b_a (m^2) are a slope and y-intercept from calibration data. These two terms capture information on the solid loading of the ink and losses downstream of the measurement point, as well as the droplet size distribution and optical configuration. With perfect impaction efficiency and dense microstructure, the y-intercept term would go to zero, and the slope term would be a pure correlation coefficient relating the amount of light scattered per volume of solid in the aerosol droplets. In addition to cross-sectional area, a congruent relationship was demonstrated between LDM and conductance for conductive inks. These prior findings provide the foundation for the present work, which shifts the focus to high rate sampling to spatially correlate print quality within a printed component, rather than simply averaging deposition rate over the entire part as done previously.

3. Materials and Methods

3.1. Inks and Materials

All experiments for this study used an ink formulated from UTD-Ag40X from UT Dots, Inc., a dispersion of 40% wt. silver nanoparticles in xylenes. Terpeneol and additional xylenes

were added to produce an ink with the ratio 2:7:1 v/v UTD-Ag40X/xylenes/terpineol. Glass microscope slides were used as the substrates for all printing experiments to provide a well-defined baseline for measurements. Prior to characterization, the silver nanoparticle test prints were sintered at 250 °C for 1 hr on a hotplate.

3.2. Aerosol Jet Printing and Optics Instrumentation

A custom, home-built aerosol jet printer was used for all experiments. This machine uses a 1.65 MHz ultrasonic atomizer for aerosol generation. A Python program was written to control the machine and record data related to deposition rate. All samples were printed with a 200 μm plastic tapered nozzle (Nordson EFD), with printhead and cartridge temperatures of 60 °C and 20 °C, respectively. Unless otherwise noted, the carrier and sheath gas flow rates were set to 18 and 90 sccm, respectively.

During aerosol jet printing, fluctuations in the aerosol characteristics can lead to short-term variation in deposition rate. To detect these fluctuations during printing, an optics cell is integrated with the printing system upstream of the printhead to measure light scattering from the aerosol stream (Fig. 1a). As shown in Fig. 1b, this optics cell includes fiber optic connections to bring in light from a laser source, and couple scattered light to a photodetector. This optics cell contained one transparent window for light input and a second for collecting scattering measurements at a 60° forward scattering angle. The light source was a 30 mW, 940 nm laser diode, and scattering power measurements were collected using a fiber-coupled InGaAs photodiode and transmitted back to the Python software via a USB interface. While this basic configuration has been demonstrated in our previous work [42], the crucial distinction here is that higher sampling rate and underlying software allows the scattering measurement to be correlated with the printhead position. When a defect is introduced into a serpentine toolpath,

causing low deposition for one section of the pattern, the scattering measurement can be mapped to position for visualization (Fig. 1c), demonstrating the concept that light scattering measurements with <1 s intervals can provide localized information about print outcomes.

3.3. Characterization methods

Cross-sectional area measurements were taken using a Zygo NewView™ 9000 optical profilometer. The raw measurements spanned a printed feature length of 1.7 mm, and the reported cross-sectional area is the average across the entire segment. Resistance measurements were collected with an electrical probe station employing a Keithley 2450 source meter and a 4-point probe measurement configuration.

4. Results and Discussion

4.1. Mapping Deposition Rate to Cartesian Space

In many printed electronics applications, a localized defect can put a device out of manufacturing tolerance. Overprinting can short adjacent lines with narrow spacing, while under-printing results in potential pinholes (for dielectrics) or higher resistors (for conductors), or in the extreme case open connections. Knowledge of local variations in printing – for example, not simply whether a 10 min print exhibits 1% average deviation from a target, but that it exhibits a discontinuity for 1 s during printing – is critical to developing an informed and rational response. Moreover, different regions of a complex electronic assembly have different tolerances – while contact pads can tolerate variation in properties, the same variation on high density interconnects could result in complete failure. Thus, having foreknowledge of a defect's location, without post-print inspection and electrical testing, would allow manufacturing engineers to rapidly determine if a print is out of spec. In this section, the positional accuracy of

light scattering measurements is examined over sub-second time intervals to provide a robust and quantitative evaluation of the basic concept.

A single 60 mm long line was printed at a print speed of 6 mm/s, and data on both the carrier gas flow rate and scattering power were measured at 125 ms intervals over the course of this 10 s print. Cross-sectional area measurements, line widths, and electrical measurements were collected at 3 mm intervals along the full length of the print, each representing a time interval of 500 ms. To simulate a spatially localized defect, a Python script was employed to drop the carrier gas flow rate for 1.5 s near the beginning of the print. In Fig. 2, the LDM and cross-sectional areas are compared at 500 ms intervals. Because the scattering measurements are taken upstream of the nozzle exit, there appeared to be approximately 250 ms of latency between measured and actual deposition rate, representing both latency between the motion system and optics instrumentation and the aerosol's time of travel between the optics cell and the substrate. With this latency accounted for, the plot shown in Fig. 2a indicates that the strong relationship between LDM and cross-sectional area holds even at very short time intervals.

Regarding the defect creation technique, while the decrease in carrier gas flow rate did drop the deposition rate in a somewhat artificial manner, the scattering measurement – and hence the aerosol volume fraction – also decreased and remained lower even after the carrier gas flow rate had returned to its baseline value. This strengthens the notion that carrier gas flow rate by itself is an insufficient predictor of deposition rate. All three parameters – carrier gas flow rate, scattering power, and LDM – are plotted together in the Supplemental Information (Fig. S1).

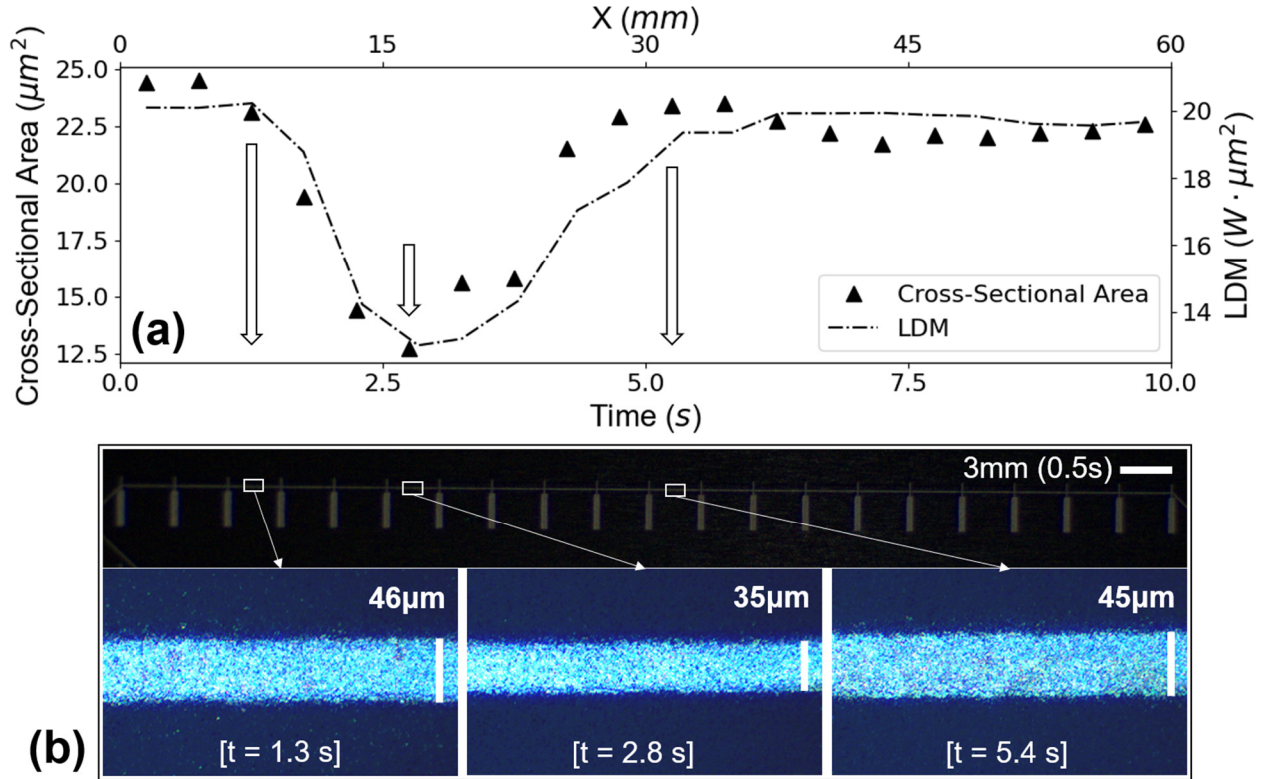


Fig. 2. (a) Cross-sectional area and linear deposition metric plotted over time and X-position at approximately 500 ms intervals over the 10 s print, demonstrating the utility of light scattering measurements for tracking deposition rate at sub-second time intervals. (b) Image of the full printed line segment (top), with microscope images before defect initiation (lower-left), at defect maximum (middle), and after defect recovery (right).

Given that resistance is a function of cross-sectional area in (5), a similar relationship is anticipated between light scattering measurements and length-normalized conductance. In the following two equations, R is resistance (Ω), ρ is resistivity ($\Omega \text{ m}$), L is length (m), A is cross-sectional area (m^2), and c is the length-normalized conductance ($\Omega^{-1} \text{ m}$). In (6), c is equated with LDM (W m^2) via linear fit parameters m_c ($\text{W}^{-1} \Omega^{-1} \text{ m}^{-1}$) and b_c ($\Omega^{-1} \text{ m}$).

$$R = \frac{\rho L}{A} = \frac{L}{c} \quad (5)$$

$$c = LDM * m_c + b_c \quad (6)$$

This relationship is analogous to (4), except that m_c and b_c capture information on the resistivity in addition to cross-sectional area, eliminating the need to obtain both cross-sectional area and electrical measurements to predict resistance.

The results shown in Fig. 3 confirm the linear relationship between LDM and length-normalized conductance. In Fig. 3a, the two variables are plotted over both time and position. At each 500 ms interval, both measurements qualitatively line up well, although there was an approximate 5% discrepancy between deposition rate and LDM before and after the defect. More quantitatively, Fig. 3b contains a line of best fit of length-normalized conductance as a function of LDM. The coefficient of determination (r^2) of this data over the whole 10 s interval is 0.914, a strong linear fit for this sampling duration. These results demonstrate that light scattering measurements can be matched with positional coordinates and be used to provide high-fidelity data on deposition rate over short time intervals, forming a strong foundation for in-situ qualification of AJP.

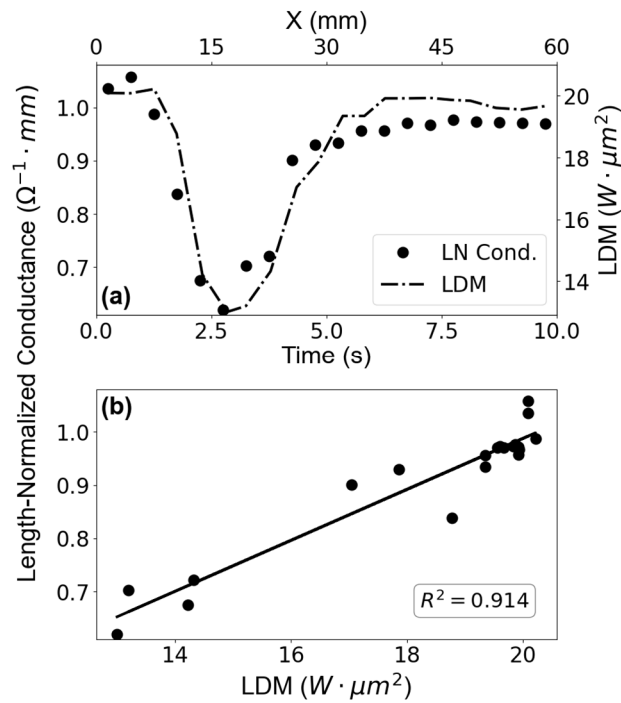


Fig. 3. (a) A comparison of measured conductance normalized to length (LN Cond.) and LDM at 500 ms intervals over the full 10 s print. (b) Line of best fit with LDM as a predictor of length-normalized conductance, verifying that a strong linear relationship can be expected for print durations on the timescale of seconds.

4.2. Prediction of Electrical Properties

4.2.1. Serial Resistive Elements

In prior work, light scattering measurements have been linked to the deposition rate and electrical conductance, but only averaged over an entire print and for a specified sample geometry [42]. The demonstration in the preceding section encourages the generalization of this to short time scales and arbitrary geometries – in effect, that the linear deposition metric can be employed as a finite element to predict resistance of features printed with AJP. Material

deposited by AJP can be conceptualized as a continuous, conductive wire with varying cross-sectional area. In this case, resistance is represented by the integral

$$R_{tot} = \int_0^L \frac{\rho}{A(s)} ds = \lim_{N \rightarrow \infty} \sum_{i=1}^N \frac{\rho}{A_i} \Delta s_i \quad (7)$$

where R_{tot} is the total resistance (Ω) of the wire of length L (m) extending in the s-direction, ρ is the resistivity ($\Omega \cdot m$), and A is the cross-sectional area (m^2). In the simplest terms, this definition is nothing more than the familiar equation for resistors in series $R_{tot} = R_1 + R_2 + \dots + R_N$. If the length interval between cross-sectional area measurements is sufficiently small, a close approximation of the true resistance can be made.

The employed measurement frequency of approximately 125 ms was expected to be adequate to approximate the integral in (7). Tying the linear deposition metric into (7), the approximation of total resistance, R_{tot} (Ω), becomes

$$R_{tot} = \sum_{i=1}^N \frac{l_i}{LDM_i * m_c + b_c} \quad (8)$$

where LDM_i is the linear deposition metric ($W m^2$) over segment i and l_i is the length of segment i . The fit coefficients m_c and b_c are obtained from a separate calibration print and equate LDM with length-normalized conductance, having units $W^{-1} \Omega^{-1} m^{-1}$ and $\Omega^{-1} m$, respectively. Following this hypothesis, any continuous feature printed by an aerosol jet printer can be approximated using real-time light scattering data, in addition to historical data correlating scattering measurements to electrical properties.

Putting this to the test, a series of two consecutive prints were performed. The first was a calibration print to back out the precise relationship between LDM and length-normalized

conductance by finding the slope and y-intercept, m_c and b_c . The toolpath used to back out these values was a generic, rectangular bar and is discussed in further detail in the Supplemental Information (Section SI 2.) This curve is similar in nature to the one shown in Fig. 3b, except the full print took place over approximately 20 min, rather than 10 s, to obtain a more reliable approximation for the fit parameters. In the second print, a multitude of serpentine patterns were printed over the course of about 35 min. In both prints, the feed rate and carrier gas flow rate remained the same throughout each print, so the resulting variation in deposition rate results solely from fluctuations in aerosol volume fraction. The measured resistances of each of these prints are plotted in Fig. 4a, alongside the predicted resistances calculated using (8).

The predicted resistances line up closely with the measured results, demonstrating that light scattering measurements capture the differences in deposition rate throughout each individual device (Fig. 4b). The predictions tend high by $\sim 10\%$ across the sample set. Because this inaccuracy was consistent throughout the whole print, measurement drift of the optics cell is unlikely. Rather, this difference is attributed to the different sample geometry between the calibration pattern (Fig. S2b) and the test pattern, which has only a single pass serpentine trace with higher resistance by a factor of ~ 50 . Better matching the calibration print geometry to the test prints is thus a promising route to address this, and the modest error despite the different resistance range illustrates the versatility of this approach.

Regardless, light scattering measurements provide a new data stream to aid with quality control for point-to-point resistance measurements. Additionally, with stable definition of the calibration fit parameters, (8) can inform print design and printing parameter selection. Using data from a single calibration print, a researcher or engineer could preemptively determine the

flow rate, print speed, and number of layers to target electrical resistance for an arbitrary pattern geometry, eliminating considerable empirical guesswork and iterative optimization.

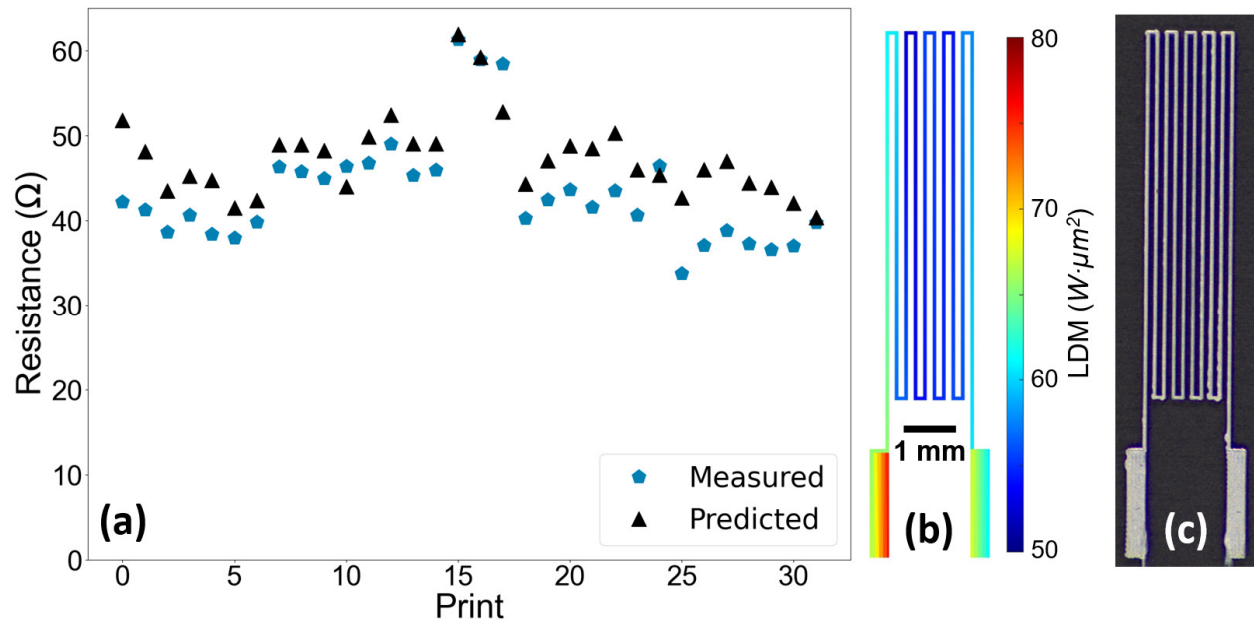


Fig. 4. (a) Comparison of measured resistances against resistances predicted using (8), verifying that the 125 ms measurement frequency of light scattering measurements can be leveraged to build finite elements capable of predicting bulk resistance of a printed device. (b) LDM colormap and (c) image of one serpentine pattern printed in this test, demonstrating enhanced data visualization beyond visual inspection.

4.2.2. Sheet Resistance

In many printed electronics applications, sheet resistance or film thickness are often the most critical design parameters. Here, a mathematical model for predicting sheet resistance is built using light scattering readings. As shown in the previous sections, LDM is an excellent proxy for the cross-sectional area of a line printed via AJP. In the equation for a continuous wire

(7), cross-sectional area appears directly, and LDM was substituted without further modification. On the other hand, the general equation for sheet resistance depends only upon resistivity and thickness. In (9), R_S is sheet resistance (Ω/\square), ρ is resistivity ($\Omega\cdot\text{m}$), and t is the thickness (m). To build a predictive equation for sheet resistance using LDM, the cross-sectional area of a single printed line must be introduced. The exact formulation could vary depending on the toolpath setup, but for a print with outside dimensions much larger than the line resolution and with an evenly spaced infill pattern of overlapping lines, the quotient of infill pitch over cross-sectional area can be substituted in place of thickness. Ultimately, this substitution results in (10), averaging LDM in localized regions to estimate average sheet resistance over the whole print. A more complete derivation may be found in the Supplemental Information Section SI 3.

$$R_S = \frac{\rho}{t} \quad (9)$$

$$R_S = \frac{1}{NM} \sum_{i=1}^N \sum_{j=1}^M \frac{d}{LDM_{ij} * m_c + b_c} \quad (10)$$

In (10), R_S is sheet resistance (Ω/\square), d is the infill pitch (m), and m_c and b_c are collected separately in a calibration print and equate LDM with length-normalized conductance, with units $\text{W}^{-1} \Omega^{-1} \text{m}^{-1}$ and $\Omega^{-1} \text{m}$, respectively. These two parameters are the same used in (8) to predict resistance and can be obtained from the same calibration print. To average sheet resistance of a single layer (and thickness by proxy) over the full region, the print is discretized into $M \times N$ regions in the XY plane.

To test this experimentally, 5x5 mm square pads were printed using a conductive silver nanoparticle ink over the course of about 90 min. A simple rectilinear infill pattern was employed with a pitch of 40 μm , following a raster motion back and forth in the X-direction for a

single layer. Each individual line was approximately 80 μm wide, so the 40 μm pitch allowed for substantial overlapping. A full diagram for the toolpath is shown in Fig. S3. The values for m_c and b_c were obtained from a separate calibration print performed immediately before the 5x5 mm squares using the same generic pattern as in the previous section (as detailed in Supplemental Information Section S I2). After sintering, resistance measurements were collected from each conductive square using the Van der Pauw method (Fig. S4). Two measurements were taken from each square pad, each measurement rotated 90° from the other to account for any anisotropy. Using both measurements, the sheet resistance for each square pad was calculated.

With physical measurements completed, a Python script was used to predict sheet resistance using (10) and available light scattering data. A comparison of measured and predicted sheet resistance values is shown in Fig. 5a. Generally, the predictions were close to the actual values but tended 5-10% high. A substantial degree of anisotropy in bulk electrical properties was present in all the prints, most probably due to localized thickness variations caused by the infill pattern. The film thickness was on the order of 1 μm , fluctuating typically ± 400 nm with the raster pattern. Resistance measured perpendicular to these peaks and valleys was notably higher than resistance measured parallel to them (Fig. S5). By itself, LDM does not provide detailed insight into the cross-sectional geometry (thickness, width, profile, etc.) of a single printed line, only the cross-sectional area. Eq. (10) simply expresses volume conservation and has no modality to account for effects of directional thickness variation on sheet resistance. Thus, it requires a smooth, consistent film comprised of overlapping printed lines for optimally accurate predictions of sheet resistance, with ink leveling dependent on both the ink properties and printing parameters.

If more accurate sheet resistance predictions are required, the LDM data could be employed to build a 3D solid model, which could then be fed into an electrostatics solver. This would additionally require foreknowledge of the cross-sectional morphology of a single printed line as a function of sheath and carrier gas flow rates, aerosol volume fraction, and print speed for a given ink to build a mathematical approximation of the cross-sectional geometry. However, in its simplicity, (10) was able to give reasonably accurate approximations of sheet resistance, increasing the breadth of light scattering measurements as a tool for in-situ qualification in aerosol jet printing.

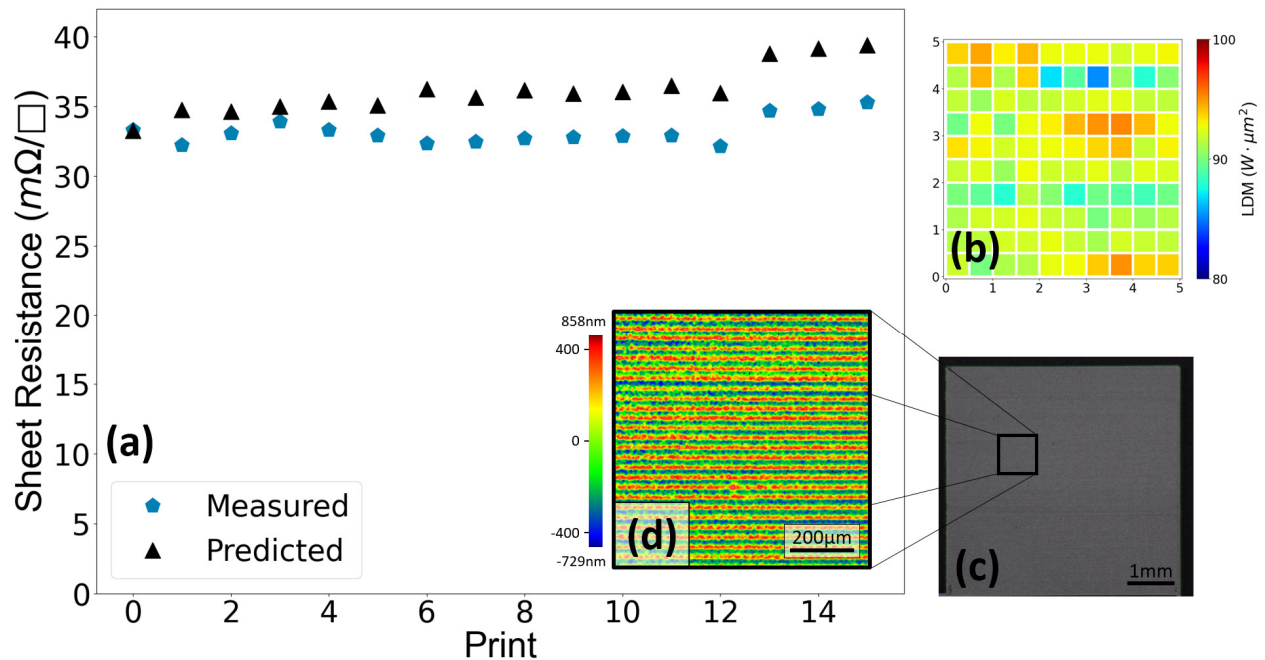


Fig. 5. (a) Comparison of measured sheet resistance values for a printed 5x5 mm square pattern, compared with values predicted by (10). (b) Color map of LDM values discretized by X and Y position alongside (c) an image of the completed print. (d) Optical profilometry data showing the presence of localized thickness variation resulting from the rectilinear toolpath, causing anisotropic bulk electrical properties.

4.3. Print Repair

Thus far, light scattering measurements have proven an effective data stream for predicting resistance over sub-second timescales. The high positional accuracy of scattering measurements shown in previous sections could support a form of post-hoc print repair, acting as a closed-loop control system. Due to its additive nature, repair with AJP alone would of course be limited to filling in low spots. Mathematically, the objective in this case is to achieve a uniform cross-sectional area across the full print. Where initially inadequate material deposition is detected, additional layers would be selectively printed to reach this objective. Cross-sectional area would be summed over multiple printed layers as

$$A_i = \sum_{j=1}^M A_j = \sum_{j=1}^M [LDM_j * m_A + b_A] \quad (11)$$

where A_i is the total cross-sectional area of segment i (m^2) and A_j and LDM_j are respectively the cross-sectional area (m^2) and linear deposition metric ($W m^2$) of each subsequent repair layer over the number of layers, M , within segment i . Again, m_A and b_A are employed to relate LDM and cross-sectional area via a linear fit. From an electronics perspective, the equivalent relationship would be the summation of resistors in parallel, $R_i^{-1} = R_1^{-1} + R_2^{-1} + \dots + R_M^{-1}$.

Replacing cross-sectional area with length-normalized conductance, the relationship becomes

$$c_i = \sum_{j=1}^M c_j = \sum_{j=1}^M [LDM_j * m_c + b_c] \quad (12)$$

where c_i is the total length-normalized conductance within segment i ($\Omega^{-1} m$). Likewise, c_j and LDM_j are the length-normalized conductance ($\Omega^{-1} m$) and linear deposition metric ($W m^2$) over M repair layers. Again, m_c and b_c are employed to equate LDM and length-normalized

conductance via a linear fit. Incorporating this with the previous definition using LDM in (8), the series resistance of a print with multiple layers would be

$$R_{tot} = \sum_{i=1}^N \frac{l_i}{\left[\sum_{j=1}^M (LDM_j * m_c + b_c) \right]_i} \quad (13)$$

with the linear deposition rate of each pass in segment i represented by LDM_j . This general equation may be extended to any print with any parallel adjoining features – basic examples being any print with multiple layers or a rectangle with an overlapping infill pattern.

To demonstrate this repair functionality, resistance measurements were compared across three groupings of 20 mm long, single-pass lines. The target LDM at the initiation of each print was $10 \text{ W } \mu\text{m}^2$. In two of these three groups, defects were induced via Python script by dropping the carrier gas flow rate for a random time between 4-8 s at a randomized position in the print and then returning to the baseline flow rate, in an identical manner to Section 4.1. In one of these two groups, a repair print was attempted, while the other was left unaltered. To achieve a uniform cross-sectional area across the whole repair print, multiple passes at a lower LDM of $1.1 \text{ W } \mu\text{m}^2$ were selectively deposited on each of the repair prints. The LDM was reduced by decreasing the carrier flow rate from 18 sccm to 13 sccm and by increasing the feed rate from 1 mm s^{-1} to 5 mm s^{-1} . A Python script was written to automatically identify the regions with inadequate deposition, determine the number of additional layers to fill them in given a target LDM, and generate toolpaths to enact the repair. This methodology is depicted in Fig. 6a. Lastly, the third group was left without induced defects to act as a control.

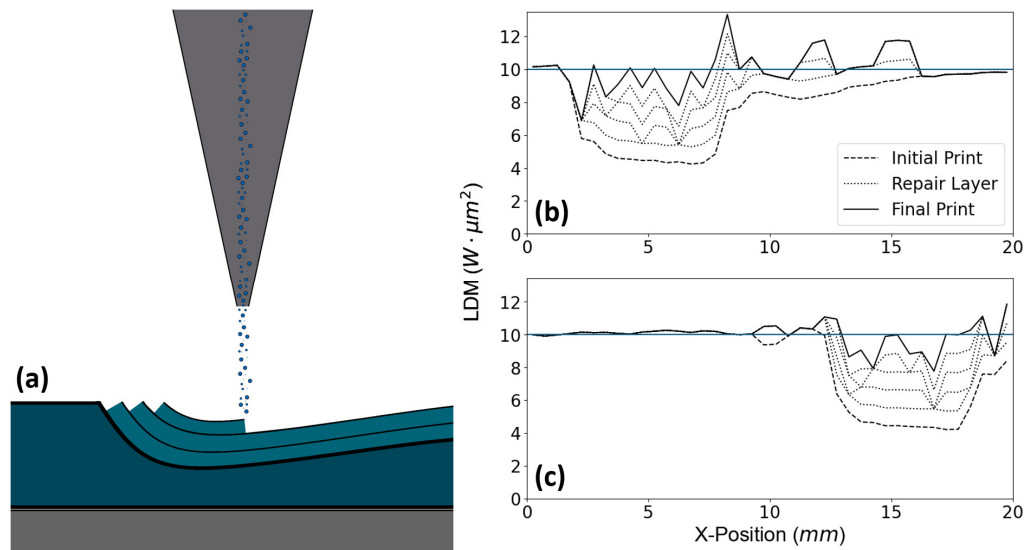


Fig. 6. (a) Diagram depicting the print repair method, with a region of inadequate material deposition being filled in with multiple light passes to reach consistent thickness throughout the whole print. (b, c) Cumulative LDM – including the initial pass and all repair layers – mapped over X-position for two repaired prints targeting a constant LDM over the full print (blue line). In (b), the defect occurs near the start of the print, while in (c) the material deficiency appears later, thus requiring a unique toolpath for repair.

The randomized defect creation script resulted in printed lines with distinct initial LDM profiles over the full length of the print. This is demonstrated in the plots of Fig. 6b and Fig. 6c, showing the accumulated LDM at increments on the full print, starting with the initially defective layer and including each of the repair layers. For the print shown in Fig. 6c, the defect develops much later than the defect shown in Fig. 6b and is not fully recovered from. Despite these differences in the initial print, the measured conductance of these two prints after repair were both within 5% of the average conductance of the control prints with no defect introduced, demonstrating the success of the repair calculation script and the methodology in general. The same goes for the other initially defective, post-repaired prints, as shown in Fig. 7. On the other

hand, the conductance of the printed lines with a randomly induced defect without follow-up repair layers averaged 42% lower than the mean conductance of the lines with no defect.

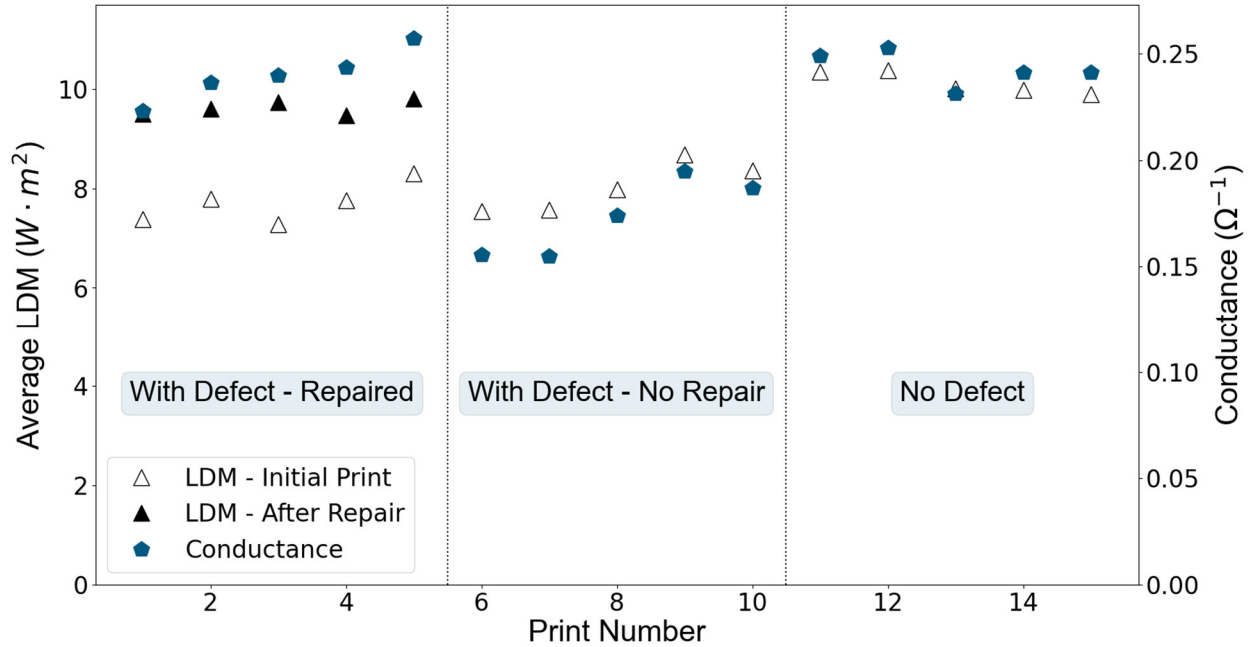


Fig. 7. Conductance and average LDM of three groups of 20 mm printed lines, with two groups containing randomly induced defects and one control group without induced defects. Results from the first group indicate successful repairs – initial LDM values are similar to the prints with induced defects, while the post-repair LDM and measured conductance values are level with the control group.

It bears noting that the defect creation demonstrated here is designed to challenge the timescale for localization and repair. A brief, acute defect is the primary concern for this work, because it strongly impacts electronic functionality and is not handled by previous quality monitoring strategies. Moreover, the repair method could be adapted depending on materials and device design. While this method used a constant deposition rate and relied heavily on the machine's shutter mechanism to print multiple layers, there is design freedom to vary the LDM

via carrier gas flow rate or print speed to minimize shuttering and printing passes. The ideal repair strategy would depend heavily on the application and the ink properties, primarily on the interaction of carrier flow rate and print speed with line resolution. While this method can of course only address under-printing defects, coupling with a subtractive method such as laser ablation could support broader applications. Regardless of the repair type, these results demonstrate that the real-time nature of light scattering measurements can support a data-rich, smart manufacturing process to enable robust quality control measures in a production environment. This could take the form of a digital twin, and a more sophisticated model could potentially account for overlap and leveling of traces to generate a 3D model of the manufactured part based on process data [47], incorporating not just the deposition rate but additional print characteristics such as resolution and line morphology. Furthermore, electronics repair using AJP could be generalized using this technique by feeding profilometry or image data to the repair calculation script, for example to achieve thickness uniformity and pinhole filling in dielectric films, or to automate conductive trace repair for printed circuit boards.

5. Conclusions

Fundamentally, this work demonstrates two new applications for light scattering measurements in AJP – data-driven quality control and physics-based process design. Regarding the former, light scattering measurements have been shown here to provide meaningful data on <1 s timescales, allowing them to be spatially correlated to the tool head position. This supports an extensive data record for each printed part that captures process parameters, spatial position, and a prediction of deposition rate. This enables operators and quality assurance personnel to locate the position of a potential defect within a printed part, and thus make a more informed and sophisticated determination of the defect criticality. Complex electronic assemblies have regions

with disparate sensitivity to fluctuations in deposition rate, and this methodology allows for high fidelity in-situ qualification with a runway to continued improvement in sampling rate. Because light scattering power represents the aerosol volume fraction, a physical parameter missing from other measurement systems, the volume of material deposited can be reliably tracked. Provided a calibration curve, the LDM is related directly to both cross-sectional area and length-normalized conductance, and can thus be substituted into relevant equations to predict functionality. This was demonstrated here for both point-to-point resistance and sheet resistance. Calibration curves were developed in tandem with the printed devices to eliminate print-to-print variability related to impaction efficiency or droplet size [46], which is attributed to suboptimal hardware design of custom-built printer components.

Future work should address the aforementioned batch-to-batch variability in the relationship of LDM to the true linear deposition rate, which could reasonably arise from second order effects influencing impaction efficiency or droplet size, such as temperature. Once this limitation is fully addressed, the mutable, physics-based approach for designing prints shown here will be generalizable and transferrable. For example, to print a film with a specified thickness, key process parameters including flow rate, print speed, layer number, and line pitch can readily be calculated prior to printing using the constitutive equation for film thickness. Combined, these two features provide a compelling foundation to integrate more advanced digital tools with the AJP process. For example, 3D digital twins of the printing process could generalize this capability to more complex patterns with diverse electronic functionality. The light scattering approach could also work in tandem with imaging-based solutions [34,38,48], which would simultaneously collect morphological data, such as line width and overspray, and provide independent detection of shorts and discontinuities. Quality control is a broad challenge across

additive manufacturing, and this work demonstrates light scattering with <1 s sampling as a viable approach to real-time quality monitoring of AJP, allowing spatial localization and repair of defects along with direct prediction of electronic functionality.

References

- [1] W.E. Frazier, Metal Additive Manufacturing: A Review, *J. Mater. Eng. Perform.* 23 (2014) 1917–1928. <https://doi.org/10.1007/s11665-014-0958-z>.
- [2] T. DebRoy, H.L. Wei, J.S. Zuback, T. Mukherjee, J.W. Elmer, J.O. Milewski, A.M. Beese, A. Wilson-Heid, A. De, W. Zhang, Additive manufacturing of metallic components – Process, structure and properties, *Prog. Mater. Sci.* 92 (2018) 112–224. <https://doi.org/10.1016/j.pmatsci.2017.10.001>.
- [3] S.K. Everton, M. Hirsch, P. Stravroulakis, R.K. Leach, A.T. Clare, Review of in-situ process monitoring and in-situ metrology for metal additive manufacturing, *Mater. Des.* 95 (2016) 431–445. <https://doi.org/10.1016/j.matdes.2016.01.099>.
- [4] T. Rahman, L. Renaud, D. Heo, M. Renn, R. Panat, Aerosol based direct-write micro-additive fabrication method for sub-mm 3D metal-dielectric structures, *J. Micromechanics Microengineering* 25 (2015) 107002. <https://doi.org/10.1088/0960-1317/25/10/107002>.
- [5] E.S. Rosker, M.T. Barako, E. Nguyen, D. DiMarzio, K. Kisslinger, D.-W. Duan, R. Sandhu, M.S. Goorsky, J. Tice, Approaching the Practical Conductivity Limits of Aerosol Jet Printed Silver, *ACS Appl. Mater. Interfaces* 12 (2020) 29684–29691. <https://doi.org/10.1021/acsami.0c06959>.
- [6] X. Konstantinou, N. Sturim, J.D. Albrecht, P. Chahal, J. Papapolymerou, A Power-Efficient Compact Ku-Band System-on-Antenna Module with Chip-First Package Integration, in: 2023 IEEE Radio Wirel. Symp. RWS, IEEE, Las Vegas, NV, USA, 2023: pp. 125–128. <https://doi.org/10.1109/RWS55624.2023.10046346>.
- [7] R. Eckstein, T. Rödlmeier, T. Glaser, S. Valouch, R. Mauer, U. Lemmer, G. Hernandez-Sosa, Aerosol-Jet Printed Flexible Organic Photodiodes: Semi-Transparent, Color Neutral, and Highly Efficient, *Adv. Electron. Mater.* 1 (2015) 1500101. <https://doi.org/10.1002/aelm.201500101>.
- [8] M.T. Rahman, A. Rahimi, S. Gupta, R. Panat, Microscale additive manufacturing and modeling of interdigitated capacitive touch sensors, *Sens. Actuators Phys.* 248 (2016) 94–103. <https://doi.org/10.1016/j.sna.2016.07.014>.
- [9] D. Zhao, T. Liu, M. Zhang, R. Liang, B. Wang, Fabrication and characterization of aerosol-jet printed strain sensors for multifunctional composite structures, *Smart Mater. Struct.* 21 (2012) 115008. <https://doi.org/10.1088/0964-1726/21/11/115008>.
- [10] C. Wang, G.-Y. Hong, K.-M. Li, H.-T. Young, A Miniaturized Nickel Oxide Thermistor via Aerosol Jet Technology, *Sensors* 17 (2017) 2602. <https://doi.org/10.3390/s17112602>.
- [11] K.T. Fujimoto, J.K. Watkins, T. Phero, D. Litteken, K. Tsai, T. Bingham, K.L. Ranganatha, B.C. Johnson, Z. Deng, B. Jaques, D. Estrada, Aerosol jet printed capacitive strain gauge for soft structural materials, *Npj Flex. Electron.* 4 (2020) 32. <https://doi.org/10.1038/s41528-020-00095-4>.
- [12] K. Parate, S.V. Rangnekar, D. Jing, D.L. Mendivelso-Perez, S. Ding, E.B. Secor, E.A. Smith, J.M. Hostetter, M.C. Hersam, J.C. Claussen, Aerosol-Jet-Printed Graphene

- Immunosensor for Label-Free Cytokine Monitoring in Serum, *ACS Appl. Mater. Interfaces* 12 (2020) 8592–8603. <https://doi.org/10.1021/acsami.9b22183>.
- [13] C. Fisher, L.N. Skolrood, K. Li, P.C. Joshi, T. Aytug, Aerosol-Jet Printed Sensors for Environmental, Safety, and Health Monitoring: A Review, *Adv. Mater. Technol.* 8 (2023) 2300030. <https://doi.org/10.1002/admt.202300030>.
- [14] L.J. Deiner, T. Jenkins, T. Howell, M. Rottmayer, Aerosol Jet Printed Polymer Composite Electrolytes for Solid-State Li-Ion Batteries, *Adv. Eng. Mater.* 21 (2019) 1900952. <https://doi.org/10.1002/adem.201900952>.
- [15] L.J. Deiner, T. Jenkins, A. Powell, T. Howell, M. Rottmayer, High Capacity Rate Capable Aerosol Jet Printed Li-Ion Battery Cathode, *Adv. Eng. Mater.* 21 (2019) 1801281. <https://doi.org/10.1002/adem.201801281>.
- [16] C. Hollar, Z. Lin, M. Kongara, T. Varghese, C. Karthik, J. Schimpf, J. Eixenberger, P.H. Davis, Y. Wu, X. Duan, Y. Zhang, D. Estrada, High-Performance Flexible Bismuth Telluride Thin Film from Solution Processed Colloidal Nanoplates, *Adv. Mater. Technol.* 5 (2020) 2000600. <https://doi.org/10.1002/admt.202000600>.
- [17] C. Cao, J.B. Andrews, A.D. Franklin, Completely Printed, Flexible, Stable, and Hysteresis-Free Carbon Nanotube Thin-Film Transistors via Aerosol Jet Printing, *Adv. Electron. Mater.* 3 (2017) 1700057. <https://doi.org/10.1002/aelm.201700057>.
- [18] S. Lu, J.A. Cardenas, R. Worsley, N.X. Williams, J.B. Andrews, C. Casiraghi, A.D. Franklin, Flexible, Print-in-Place 1D–2D Thin-Film Transistors Using Aerosol Jet Printing, *ACS Nano* 13 (2019) 11263–11272. <https://doi.org/10.1021/acs.nano.9b04337>.
- [19] G.L. Goh, H. Zhang, G.D. Goh, W.Y. Yeong, T.H. Chong, Multi-objective optimization of intense pulsed light sintering process for aerosol jet printed thin film, *Mater. Sci. Addit. Manuf.* 1 (2022) 10. <https://doi.org/10.36922/msam.26>.
- [20] K. Hong, S.H. Kim, A. Mahajan, C.D. Frisbie, Aerosol Jet Printed p- and n-type Electrolyte-Gated Transistors with a Variety of Electrode Materials: Exploring Practical Routes to Printed Electronics, *ACS Appl. Mater. Interfaces* 6 (2014) 18704–18711. <https://doi.org/10.1021/am504171u>.
- [21] L. Gamba, Z.T. Johnson, J. Atterberg, S. Diaz-Arauzo, J.R. Downing, J.C. Claussen, M.C. Hersam, E.B. Secor, Systematic Design of a Graphene Ink Formulation for Aerosol Jet Printing, *ACS Appl. Mater. Interfaces* 15 (2023) 3325–3335. <https://doi.org/10.1021/acsami.2c18838>.
- [22] L. Gamba, S. Diaz-Arauzo, M.C. Hersam, E.B. Secor, Aerosol Jet Printing of Phase-Inversion Graphene Inks for High-Aspect-Ratio Printed Electronics and Sensors, *ACS Appl. Nano Mater.* 6 (2023) 21133–21140. <https://doi.org/10.1021/acsanm.3c04207>.
- [23] S. Stoukatch, P. Laurent, S. Dricot, F. Axisa, L. Seronveaux, D. Vandormael, E. Beeckman, B. Heusdens, J. Destine, Evaluation of Aerosol Jet Printing (AJP) technology for electronic packaging and interconnect technique, in: 2012 4th Electron. Syst.-Integr. Technol. Conf., IEEE, Amsterdam, Netherlands, 2012: pp. 1–5. <https://doi.org/10.1109/ESTC.2012.6542067>.
- [24] T. Seifert, M. Baum, F. Roscher, M. Wiemer, T. Gessner, Aerosol Jet Printing of Nano Particle Based Electrical Chip Interconnects, *Mater. Today Proc.* 2 (2015) 4262–4271. <https://doi.org/10.1016/j.matpr.2015.09.012>.
- [25] X. Konstantinou, J.D. Albrecht, P. Chahal, J. Papapolymerou, Flexible Chip-First Millimeter-Wave Packaging Using Multiple Dielectrics, *IEEE Trans. Compon. Packag. Manuf. Technol.* 12 (2022) 682–691. <https://doi.org/10.1109/TCPMT.2022.3160626>.

- [26] S. Vella, C. Smithson, K. Halfyard, E. Shen, M. Chrétien, Integrated capacitive sensor devices aerosol jet printed on 3D objects, *Flex. Print. Electron.* 4 (2019) 045005. <https://doi.org/10.1088/2058-8585/ab59c0>.
- [27] J.A. Paulsen, M. Renn, K. Christenson, R. Plourde, Printing conformal electronics on 3D structures with Aerosol Jet technology, in: 2012 Future Instrum. Int. Workshop FIIW Proc., IEEE, Gatlinburg, TN, USA, 2012: pp. 1–4. <https://doi.org/10.1109/FIIW.2012.6378343>.
- [28] Y. Gu, D. Park, D. Bowen, S. Das, D.R. Hines, Direct-Write Printed, Solid-Core Solenoid Inductors with Commercially Relevant Inductances, *Adv. Mater. Technol.* 4 (2019) 1800312. <https://doi.org/10.1002/admt.201800312>.
- [29] M. Saeidi-Javash, W. Kuang, C. Dun, Y. Zhang, 3D Conformal Printing and Photonic Sintering of High-Performance Flexible Thermoelectric Films Using 2D Nanoplates, *Adv. Funct. Mater.* 29 (2019) 1901930. <https://doi.org/10.1002/adfm.201901930>.
- [30] K. Werum, E. Mueller, J. Keck, J. Jaeger, T. Horter, K. Glaeser, S. Buschkamp, M. Barth, W. Eberhardt, A. Zimmermann, Aerosol Jet Printing and Interconnection Technologies on Additive Manufactured Substrates, *J. Manuf. Mater. Process.* 6 (2022) 119. <https://doi.org/10.3390/jmmp6050119>.
- [31] G.L. Goh, V. Dikshit, R. Koneru, Z.K. Peh, W. Lu, G.D. Goh, W.Y. Yeong, Fabrication of design-optimized multifunctional safety cage with conformal circuits for drone using hybrid 3D printing technology, *Int. J. Adv. Manuf. Technol.* 120 (2022) 2573–2586. <https://doi.org/10.1007/s00170-022-08831-y>.
- [32] R.R. Tafoya, E.B. Secor, Understanding and mitigating process drift in aerosol jet printing, *Flex. Print. Electron.* 5 (2020) 015009. <https://doi.org/10.1088/2058-8585/ab6e74>.
- [33] K. Wang, Y.-H. Chang, C. Zhang, B. Wang, Evaluation of Quality of Printed Strain Sensors for Composite Structural Health Monitoring Applications, in: 2013.
- [34] H. Sun, K. Wang, Y. Li, C. Zhang, R. Jin, Quality Modeling of Printed Electronics in Aerosol Jet Printing Based on Microscopic Images, *J. Manuf. Sci. Eng.* 139 (2017) 071012. <https://doi.org/10.1115/1.4035586>.
- [35] R.R. Tafoya, E.B. Secor, Understanding effects of printhead geometry in aerosol jet printing, *Flex. Print. Electron.* 5 (2020) 035004. <https://doi.org/10.1088/2058-8585/aba2bb>.
- [36] Y. Gu, D. Gutierrez, S. Das, D.R. Hines, Inkwells for on-demand deposition rate measurement in aerosol-jet based 3D printing, *J. Micromechanics Microengineering* 27 (2017) 097001. <https://doi.org/10.1088/1361-6439/aa817f>.
- [37] R. Salary, J.P. Lombardi, M. Samie Tootooni, R. Donovan, P.K. Rao, P. Borgesen, M.D. Poliks, Computational Fluid Dynamics Modeling and Online Monitoring of Aerosol Jet Printing Process, *J. Manuf. Sci. Eng.* 139 (2017) 021015. <https://doi.org/10.1115/1.4034591>.
- [38] R. Salary, J.P. Lombardi, P.K. Rao, M.D. Poliks, Online Monitoring of Functional Electrical Properties in Aerosol Jet Printing Additive Manufacturing Process Using Shape-From-Shading Image Analysis, *J. Manuf. Sci. Eng.* 139 (2017) 101010. <https://doi.org/10.1115/1.4036660>.
- [39] J.P. Lombardi, R. Salary, D.L. Weerawarne, P.K. Rao, M.D. Poliks, In-Situ Image-Based Monitoring and Closed-Loop Control of Aerosol Jet Printing, in: Vol. 1 Addit. Manuf. Bio Sustain. Manuf., ASME, College Station, Texas, USA, 2018: p. V001T01A039. <https://doi.org/10.1115/MSEC2018-6487>.
- [40] R.R. Tafoya, A.W. Cook, B. Kaehr, J.R. Downing, M.C. Hersam, E.B. Secor, Real-Time Optical Process Monitoring for Structure and Property Control of Aerosol Jet Printed

- Functional Materials, *Adv. Mater. Technol.* 5 (2020) 2000781.
<https://doi.org/10.1002/admt.202000781>.
- [41] E.B. Secor, Light scattering measurements to support real-time monitoring and closed-loop control of aerosol jet printing, *Addit. Manuf.* 44 (2021) 102028.
<https://doi.org/10.1016/j.addma.2021.102028>.
- [42] J.D. Rurup, E.B. Secor, Predicting Deposition Rate and Closing the Loop on Aerosol Jet Printing with In-Line Light Scattering Measurements, *Adv. Eng. Mater.* (2023) 2201919.
<https://doi.org/10.1002/adem.202201919>.
- [43] M. Smith, Y.S. Choi, C. Boughey, S. Kar-Narayan, Controlling and assessing the quality of aerosol jet printed features for large area and flexible electronics, *Flex. Print. Electron.* 2 (2017) 015004. <https://doi.org/10.1088/2058-8585/aa5af9>.
- [44] A. Wadhwa, Run-time Ink Stability in Pneumatic Aerosol Jet Printing Using a Split Stream Solvent Add Back System, Rochester Institute of Technology, 2015.
<https://scholarworks.rit.edu/theses/8597>.
- [45] J.Q. Feng, M.J. Renn, Aerosol Jet® Direct-Write for Microscale Additive Manufacturing, *J. Micro Nano-Manuf.* 7 (2019) 011004. <https://doi.org/10.1115/1.4043595>.
- [46] A.A. Kokhanovsky, *Aerosol Optics: Light Absorption and Scattering by Particles in the Atmosphere*, in: Springer-Praxis, New York; Chichester, UK, 2008: p. 146.
- [47] J.D. Rurup, E.B. Secor, A Real-Time Process Diagnostic to Support Reliability, Control, and Fundamental Understanding in Aerosol Jet Printing, *Adv. Eng. Mater.* (2023) 2301348.
<https://doi.org/10.1002/adem.202301348>.
- [48] Y. Li, H. Sun, X. Deng, C. Zhang, H.-P. (Ben) Wang, R. Jin, Manufacturing quality prediction using smooth spatial variable selection estimator with applications in aerosol jet® printed electronics manufacturing, *IISE Trans.* 52 (2020) 321–333.
<https://doi.org/10.1080/24725854.2019.1593556>.

Supplemental Information

In-Situ Qualification and Physics-Based Process Design for Aerosol Jet Printing via Spatially Correlated Light Scattering Measurements

Jeremy D. Rurup^a, *Ethan B. Secor*^{a,*}

^a Department of Mechanical Engineering, Iowa State University, Ames, IA 50011, USA

* Correspondence to: Iowa State University, Ames, IA 50011, USA. E-mail address: esecor@iastate.edu.

KEYWORDS: additive manufacturing, printed electronics, process monitoring, hybrid electronics, digital manufacturing

SI 1. Raw Data from Manual Defect Creation (Section 4.1)

The data shown in Fig. S1 is a comparison of the raw, unaltered LDM, carrier flow rate, and scattering measurements shown in Fig. 3a. The plot shown in that figure has been sorted into 500 ms bins, with the LDM data in each bin being averaged, visually smoothing the plotted result, but otherwise not altering the data. Here, the necessity of light scattering measurements is more completely demonstrated. The defects induced for prints in Section 4.1 and Section 4.3 both involved sharply decreasing the carrier gas flow rate, resulting in a delayed decrease in the light scattering measurement – and therefore aerosol volume fraction. Despite the short duration of defect inducement, this plot shows that tracking the carrier gas flow rate by itself would have caused a substantial mismatch in the predicted and actual deposition rate.

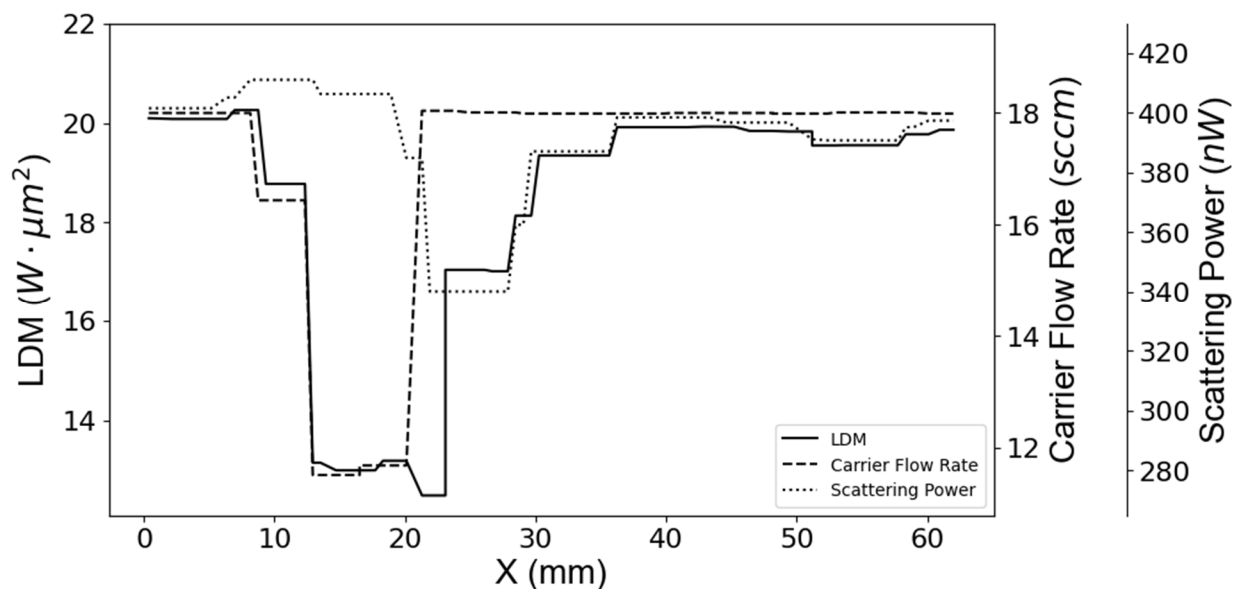


Fig. S1. Real time data comparing LDM, carrier flow rate, and scattering power over the course of the print, showing that inducing a defect by rapidly dropping the carrier flow rate leads to a delayed reduction in the aerosol volume fraction, necessitating light scattering measurements for defect detection.

SI 2. Calibration Print Data for Resistance Predictions (Section 4.2.)

For a full prediction of resistance, (8) requires external calibration data relating LDM to the length-normalized conductance of a printed line. This is achieved in Fig. S2a, by generating a line of best fit for the data, as described below. The toolpath used for the calibration pattern is shown in Fig. S2b and Fig. S2c. The pattern consists of a several layer thick, 9 mm x 160 μm rectangle with four 0.5mm measurement pads for resistance measurements via four-point probe. Atomizer voltage was manually manipulated to vary deposition rate for each print in the calibration curve. For normalizing conductance to length, the measured conductance was multiplied by the length between the two inner pads (5 mm) and divided by the number of passes

(10) to obtain a value with units of $\Omega^{-1} \text{ mm}$. Finally, a linear fit line was calculated with LDM as a predictor of these values of length-normalized conductance.

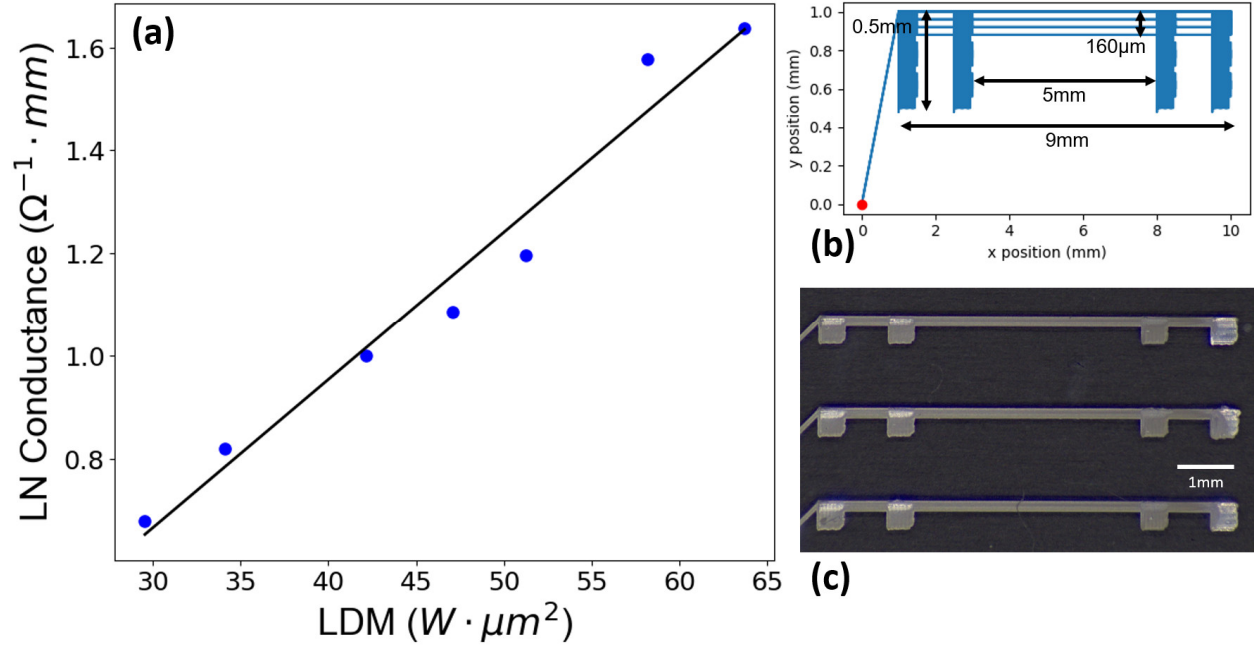


Fig. S2. (a) Calibration curve used to obtain resistance predictions for the serpentine dataset in Section 4.2.1., with regard to LDM as a predictor of measured conductance normalized to length (LN Conductance) in millimeters of printed line. (b) Diagram (X and Y axes not to scale) and (c) image of the toolpath used for calibration curve generation.

SI 3. Sheet Resistance Predictions

Thickness and Sheet Resistance Predictor Derivation

A derivation of the sheet resistance estimation in (10) is given below. With regard to the toolpath, this model assumes an evenly spaced, overlapping (pitch smaller than line width) rectilinear infill pattern, like the pattern shown in Fig. S3 and used in Section 4.2.2. The general objective is to mathematically link the cross-sectional area of a single printed line with thickness. First, the total volume V (m^3) of printed material is expressed with two equivalent equations; the

first in terms of thickness t (m) and surface area A_{surf} (m²), and the second in terms of the cross-sectional area of a single printed line A_{xs} (m²) and the total length of the toolpath L (m).

$$V = A_{surf}t = A_{xs}L$$

The next objective is reducing A_{surf} and L in terms of the pitch or infill spacing d (m) and the width of a printed region, l (m). A_{surf} is simply the product of the total length and width of the printed region, and L is the summation of all line segments. The variable N is the number of passes within the region.

$$A_{surf} = (Nd)l$$

$$L = N(l + d) \approx Nl$$

In the equation for total toolpath length L , the d term is neglected since it only affects the exterior edges of the print. Substituting both into the volume equation yields the following.

$$V = (Nd)lt = A_{xs}Nl$$

The N and l terms divide out of both sides, resulting in the thickness being expressed as shown below. Sheet resistance R_s (Ω/\square) is simply the quotient of resistivity ρ (Ω m) and thickness and is expressed below, incorporating the new equation for film thickness.

$$t = \frac{A_{xs}}{d}$$

$$R_s = \frac{\rho d}{A_{xs}}$$

From here, all that remains is introducing the LDM and calibration fit parameters for cross-sectional area and length-normalized conductance. These substitutions are shown below. These expressions will yield the thickness or sheet resistance at a given XY position.

$$t = \frac{LDM * m_A + b_A}{d}$$

$$R_s = \frac{\rho d}{LDM * m_A + b_A} = \frac{d}{LDM * m_c + b_c}$$

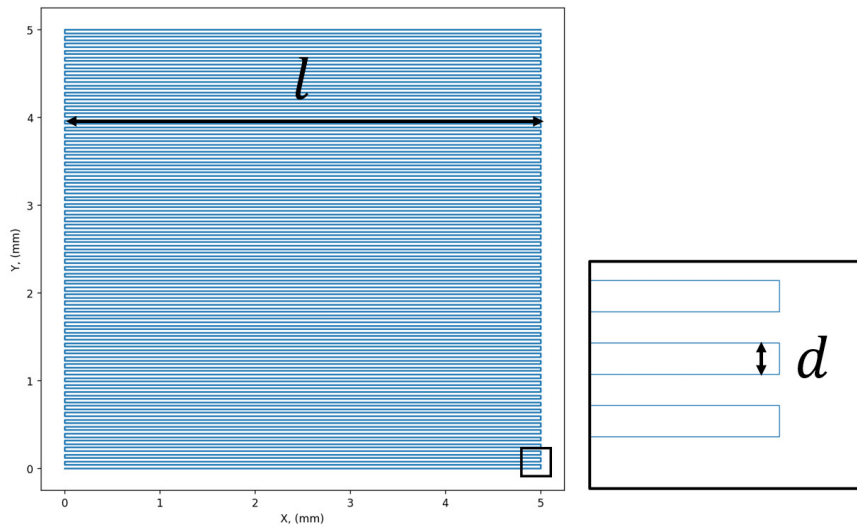


Fig. S3. The toolpath used to print conductive square for sheet resistance measurements in Section 4.2.2. This consists of a 5x5 mm square, with a uniform, 40 μm rectilinear infill pattern, making it valid for (10).

Resistance Measurements – Van der Pauw Method

The Van der Pauw method was used to collect sheet resistance measurements. For each of the squares, an electrical probe was placed in each of the four corners. Current was sourced across two adjacent probes, and voltage was measured across the remaining two, allowing for resistance to be calculated, as shown below in Fig. S4. This was repeated twice for each square – once measuring voltage perpendicular to the raster and once parallel to the raster. Sheet resistance was then calculated using both measurements. Because sheet resistance cannot be measured more locally using this setup, validation of local variations cannot be performed, and are further challenged by the fact that the calculation of sheet resistance assumes a uniform thickness. As a result, while we can show some value in estimating sheet resistance based on

process data, more sophisticated methods would be needed to account for real variations in thickness and anisotropy. As these methods would be necessary for generalizing this approach to point-to-point resistance with more complex geometries anyway, we view these as a natural next step for using in-line measurements, requiring more sophisticated modeling but leveraging the same process monitoring technology.

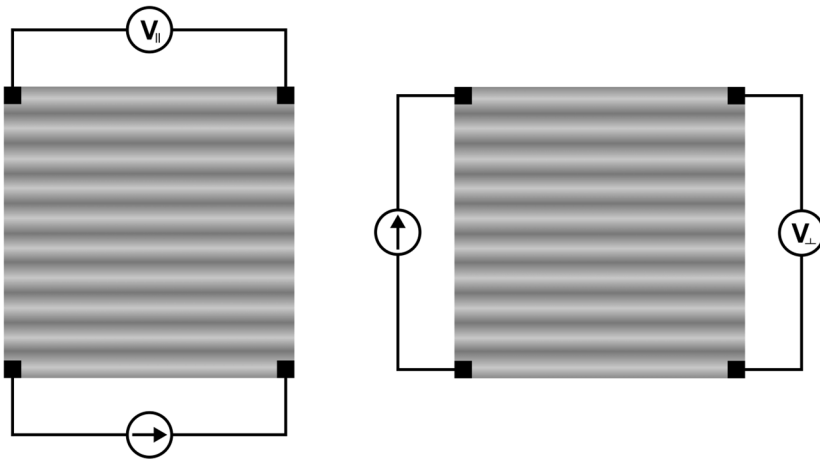


Fig. S4. Sheet resistance measurements collected via the Van der Pauw method taken parallel to the raster (left) and perpendicular to the raster (right).

In the physical prints, the resistance measurements obtained with the Van der Pauw method showed a substantial degree of anisotropy. Fig. S5 shows the raw resistance readings obtained using the Van der Pauw method both perpendicular and parallel to the infill direction.

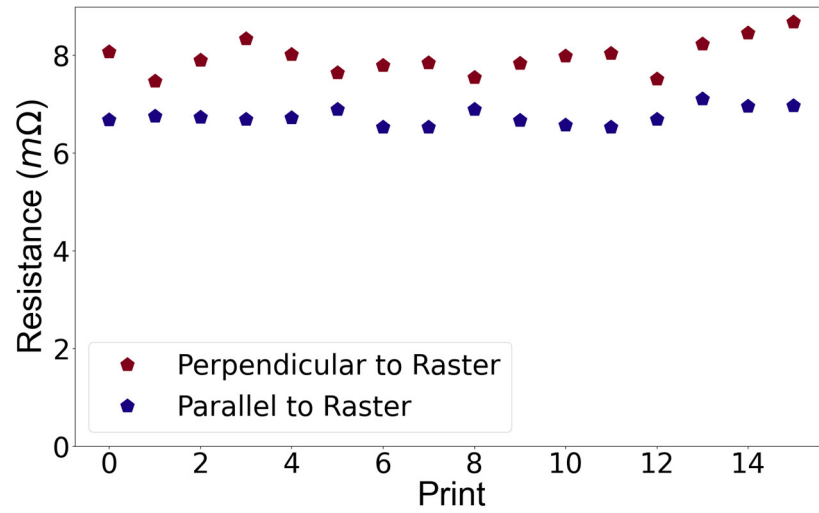


Fig. S5. Anisotropy in bulk electrical properties of the printed squares perpendicular and parallel to the raster direction of the 5x5 mm squares printed for Section 4.2.2.